



## Full paper

# Realizing stable lithium and sodium storage with high areal capacity using novel nanosheet-assembled compact CaV<sub>4</sub>O<sub>9</sub> microflowers



Xiaoming Xu, Peijie Wu, Qi Li\*, Wei Yang, Xiao Zhang, Xuanpeng Wang, Jiashen Meng, Chaojiang Niu, Liqiang Mai\*

State Key Laboratory of Advanced Technology for Materials Synthesis and Processing, International School of Materials Science and Engineering, Wuhan University of Technology, Wuhan 430070, China

## ARTICLE INFO

## Keywords:

CaV<sub>4</sub>O<sub>9</sub>  
Compact microflowers  
Stable Li/Na storage  
High areal capacity  
Increased tap density

## ABSTRACT

Realizing stable cycling performance with high areal capacity is a great challenge for metal-ion battery anodes. Achieving high areal capacity generally requires the electrode in a high active loading with increased electrode thickness, which is not beneficial to the cycling stability. In this work, novel nanosheet-assembled compact CaV<sub>4</sub>O<sub>9</sub> microflowers are firstly synthesized through a facile method, which exhibit both high areal capacity and stable cycling performance at high mass loadings. The compact microflower structure leads to an increased tap density of the electrode materials, benefiting to reduce the anode thickness at high mass loadings. Meanwhile, the assembled nanosheets maintain the nano-effects of the active materials for favorable electrochemical reactions. These merits together with the intrinsic superior electrochemical properties of CaV<sub>4</sub>O<sub>9</sub>, result in the outstanding electrochemical performance. When used as Li-ion battery anodes, a high areal capacity of ~2.5 mAh cm<sup>-2</sup> at a high mass loading of 4.4 mg cm<sup>-2</sup> is obtained, and a stable cycling over 400 cycles with the areal capacity over 1.5 mAh cm<sup>-2</sup> is demonstrated. Besides, the superior electrochemical performance at high mass loadings is also observed for Na storage. These achievements may pave the way for constructing applicable high-capacity and stable anode materials in metal-ion batteries.

## 1. Introduction

Electrochemical energy storage devices play increasingly important roles in the modern society. Lithium-ion batteries (LIBs) have dominated the market of portable electronic devices, and also gradually become the main power source for electric vehicles [1]. The increasing demand for high energy-density LIBs requires the innovations of electrode materials. Several high-capacity anode materials (such as SnO<sub>2</sub>, Fe<sub>2</sub>O<sub>3</sub>, Si, etc.) beyond commercialized graphite have received great attention [2–4]. However the serious structure degradation and fast capacity fading resulting from large volume change is a big issue [5]. The emerging sodium-ion batteries (SIBs), which are similar to LIBs in electrochemical process, are placed in a high expectation for stationary energy storage systems or smart grids in recent years, due to the high abundance and low cost of Na resource [6]. Whereas, the severe capacity fading is also one of the challenges suffered by most SIB anodes, as the larger ionic radius of Na<sup>+</sup> results in slower diffusion kinetics and even worse structure degradation of the electrodes [7,8].

In previous years, a large number of reports have demonstrated the availability of constructing nanostructured materials to address the

issue of structure degradation and fast capacity fading, since nanomaterials possess multiple advantages including shortened ion diffusion distance, larger electrode/electrolyte contact area and better strain release [5,9–13]. However, downsizing to nanoscale is actually a double-edged sword for the electrode materials in batteries. Nanomaterials, especially hollow or porous nanostructured materials are always accompanied by a low tap density [14–16], which will result in a thicker electrode and hence a decreased volumetric capacity at the same mass loading level [5,17]. On the other side, although exciting cycling performances have been achieved for high-capacity anodes at low mass loading level (~1.0 mg cm<sup>-2</sup>) [3,9,18–24], the resulting low areal capacity below the requirement for commercial application is still a key issue. The displayed long-term cycling performance at low mass loadings (corresponding to low areal capacity) can hardly be maintained in most cases when the mass loading is increased to a high level (> 3.0 mg cm<sup>-2</sup> for anode). This is because high mass loading (corresponding to high areal capacity) means thicker electrode and longer charge transport distance, which results in the limited electrolyte infiltration and increased overpotential during cycling, especially at high current densities [1,25–27]. More importantly, the thicker electrode is

\* Corresponding authors.

E-mail addresses: [qi.li@whut.edu.cn](mailto:qi.li@whut.edu.cn) (Q. Li), [mlq518@whut.edu.cn](mailto:mlq518@whut.edu.cn) (L. Mai).

more sensitive to the large volume change. And the large volumetric expansion and contraction would lead to crack or pulverization of both active materials and electrodes, causing the loss of electrical contact or even delamination of the materials from current collector, and resulting in the formation of dead material [5].

Realizing high areal capacity and stable cycling performance at high mass loadings is highly significant for the innovation of battery technology. To achieve this goal, electrode materials need to meet the following requirements: 1) a high gravimetric specific capacity and good intrinsic electrochemical reversibility; 2) small volume change during cycling to ensure small mechanical stress and structure stability; 3) a high tap density to effectively decrease the electrode thickness and shorten the charge transport pathway; 4) good electric conductivity and ion diffusion kinetics to enable the efficient transport of electrons and ions. The typical conversion and alloying reaction based anodes (such as  $\text{Co}_3\text{O}_4$ ,  $\text{Fe}_3\text{O}_4$ ,  $\text{SnO}_2$  and Si, etc.) can exhibit a high gravimetric specific capacity, but generally suffer from large volume change, which cause the instability of the electrodes, especially when the active loading is increased to a high level for high areal capacity. Different from the typical conversion reaction based anodes, vanadium oxides possess potentially smaller volume change when used as anode materials, since the valence of vanadium cannot reach zero at low voltage due to the strong V-O bond strength [28]. Meanwhile, the multivalent vanadium renders the multi-electron transfer during the electrochemical reaction, and thus high specific capacity can be achieved. However, the typical vanadium oxides (such as  $\text{V}_2\text{O}_5$ ,  $\text{V}_2\text{O}_3$ , etc.) still suffer from low electric conductivity and poor reaction kinetics [29]. Recently, our group identified a new vanadium-based anode material,  $\text{CaV}_4\text{O}_9$ , for SIBs [30], which exhibits exciting electrochemical properties and interesting Na storage mechanism. The  $\text{CaV}_4\text{O}_9$  nanowires were found to exhibit intrinsic high electronic conductivity ( $> 100 \text{ S cm}^{-1}$ ), small volume change ( $< 10\%$ ) during sodiation/desodiation, and good electrochemical reversibility due to the self-preserving effect from in situ formed  $\text{CaO}$ , which result in an excellent cycling stability for Na storage. Considering these observed superior properties, it is suggested that  $\text{CaV}_4\text{O}_9$  is a high promising anode material to realize both stable cycling performance and high areal capacity at high mass loadings.

Herein, we firstly synthesized nanosheet-assembled compact  $\text{CaV}_4\text{O}_9$  microflowers and realized both stable cycling and high areal capacity for Li and Na storage. The compact microflower structure effectively increases the space utilization and results in an increased tap density comparable to the nanowires. Meanwhile, the nanosheets maintain the nano-effects (including shorter ion diffusion distance, better strain release and more active sites) for favorable electrochemical reactions. Attributing to the increased tap density and maintained nano-effects, together with the intrinsic superior properties of  $\text{CaV}_4\text{O}_9$  (such as high electric conductivity, small volume change and excellent electrochemical reversibility), the prepared compact  $\text{CaV}_4\text{O}_9$  microflowers exhibit stable cycling performance with high areal capacity at high mass loadings, both for Li and Na storage, even without any special modification.

## 2. Experimental section

### 2.1. Materials synthesis

The compact  $\text{CaV}_4\text{O}_9$  microflowers were synthesized as follows: 1 mmol of  $\text{Ca}(\text{OH})_2$  was added into a mixed solution with 10 ml of deionized  $\text{H}_2\text{O}$  and 10 ml of  $\text{C}_3\text{H}_8\text{O}_3$  (glycerol) to form solution A. On the other side, 2 mmol of  $\text{V}_2\text{O}_5$  was dispersed in 10 ml of deionized  $\text{H}_2\text{O}$ , followed by the adding of 5 ml of  $\text{H}_2\text{O}_2$  drop by drop to form solution B. Solution A and Solution B was stirred for about 1 h separately, and then was mixed to form solution C. Solution C was further stirred for another 2 h, and then was transferred into a 50 ml Teflon-lined stainless steel autoclave. The autoclave was placed at  $200^\circ\text{C}$  for 2

days and then was cooled to room temperature naturally. The obtained dark blue precipitate from the autoclave was washed by deionized water and alcohol for several times, and dried at  $70^\circ\text{C}$  for 24 h. Finally, the product was annealed in Ar atmosphere at  $400^\circ\text{C}$  for 8 h and  $500^\circ\text{C}$  for 2 h to get the final product. When replacing the  $\text{Ca}(\text{OH})_2$  by  $\text{Sr}(\text{OH})_2$ ,  $\text{SrV}_4\text{O}_9$  microflowers can also be obtained.

### 2.2. Material characterizations

The X-ray diffraction (XRD) patterns were obtained using a Bruker D8 Discover X-ray diffractometer with  $\text{Cu K}\alpha$  radiation source. Scanning electron microscopy (SEM) images were collected on a JEOL-7100F microscope. The Oxford EDS IE250 system was used to record the energy-dispersive X-ray spectra (EDS) mapping. Transmission electron microscopy (TEM) measurements were carried out on a JEOL JEM-2100F STEM/EDS microscope at an accelerating voltage of 200 kV. Inductively coupled plasma (ICP) results were obtained using a PerkinElmer Optima 4300DV spectrometer. Thermogravimetry analysis (TGA) was performed on a Netzsch STA 449F3 simultaneous thermal analyzer in Ar. The Brunauer–Emmett–Teller (BET) surface area was calculated from nitrogen adsorption isotherms collected at 77 K using a Tristar-3020 instrument.

### 2.3. Electrochemical measurements

The electrochemical measurements were conducted by assembling 2016 coin cells in a glove box. The working electrodes were prepared using a typical coating method by mixing  $\text{CaV}_4\text{O}_9$  microflowers with acetylene black and carboxyl methyl cellulose (CMC) binder in a weight ratio of 7:2:1. The mixture was spread on a copper foil uniformly, dried at  $70^\circ\text{C}$  and then was punched into small wafers with diameter of 1.0 cm. The mass loading was controlled to be in the range from 0.5 to  $4.5 \text{ mg cm}^{-2}$ . The coin cells were assembled using Li or Na foil as the counter/reference electrode. The Celgard 2300 membrane and the Whatman glass microfiber (Grade GF/F) were used as the separator for LIBs and SIBs, respectively. The electrolyte was 1 M  $\text{LiPF}_6$  in 1:1 v/v ethylene carbonate (EC)/dimethyl carbonate (DMC) for LIBs, and 1 M  $\text{NaClO}_4$  in 1:1 v/v EC/DMC with 5% fluoroethylene carbonate (FEC) for SIBs. Galvanostatic charge/discharge measurements were carried out using a multi-channel battery testing system (LAND CT2001A). Cyclic voltammograms (CV) were recorded using an electrochemical workstation (Autolab PGSTAT 302 N).

## 3. Results and discussions

The  $\text{CaV}_4\text{O}_9$  microflowers were synthesized as illustrated in Fig. S1, which can also be applied to obtain  $\text{SrV}_4\text{O}_9$  microflowers by replacing  $\text{Ca}(\text{OH})_2$  by  $\text{Sr}(\text{OH})_2$  in solution A. The XRD results of the final products indicate the pure phase of  $\text{CaV}_4\text{O}_9$  (JCPDS: 01-070-4469) and  $\text{SrV}_4\text{O}_9$  (JCPDS: 01-070-4468), without any other impurities (Fig. 1a). It is noted that  $\text{CaV}_4\text{O}_9$  is similar to  $\text{SrV}_4\text{O}_9$  in crystal structure (Fig. S2 and Table S1). Both of them possess a layered structure with  $\text{Ca}^{2+}$  or  $\text{Sr}^{2+}$  distributed uniformly in the layers. The SEM images of  $\text{CaV}_4\text{O}_9$  (Fig. 1b) and  $\text{SrV}_4\text{O}_9$  (Fig. 1c) show the microflower morphology, which are assembled by many ultrathin nanosheets. The size of microflowers is about 2–3  $\mu\text{m}$ . EDS mappings (Fig. 1d and e) indicate the existence of Ca/Sr, V and O in the samples and the uniform distribution of the elements. The TEM and high-resolution TEM (HRTEM) images of  $\text{CaV}_4\text{O}_9$  are presented in Fig. 1f–h. From the TEM image (Fig. 1f), it is found that the microflower is solid and dense, which is beneficial to increase the tap density of the electrodes. The tap density of  $\text{CaV}_4\text{O}_9$  microflower was measured to be  $0.74 \text{ g cm}^{-3}$ , which shows a distinct increase compared to our previously reported nanowires [30] (Fig. S3 and S4), and also is comparable to that of commercialized graphite ( $0.7\text{--}1.0 \text{ g cm}^{-3}$ ) or hard carbon ( $0.5\text{--}0.8 \text{ g cm}^{-3}$ ) [31,32]. From the magnified TEM image (Fig. 1g), a large number of mesopores were

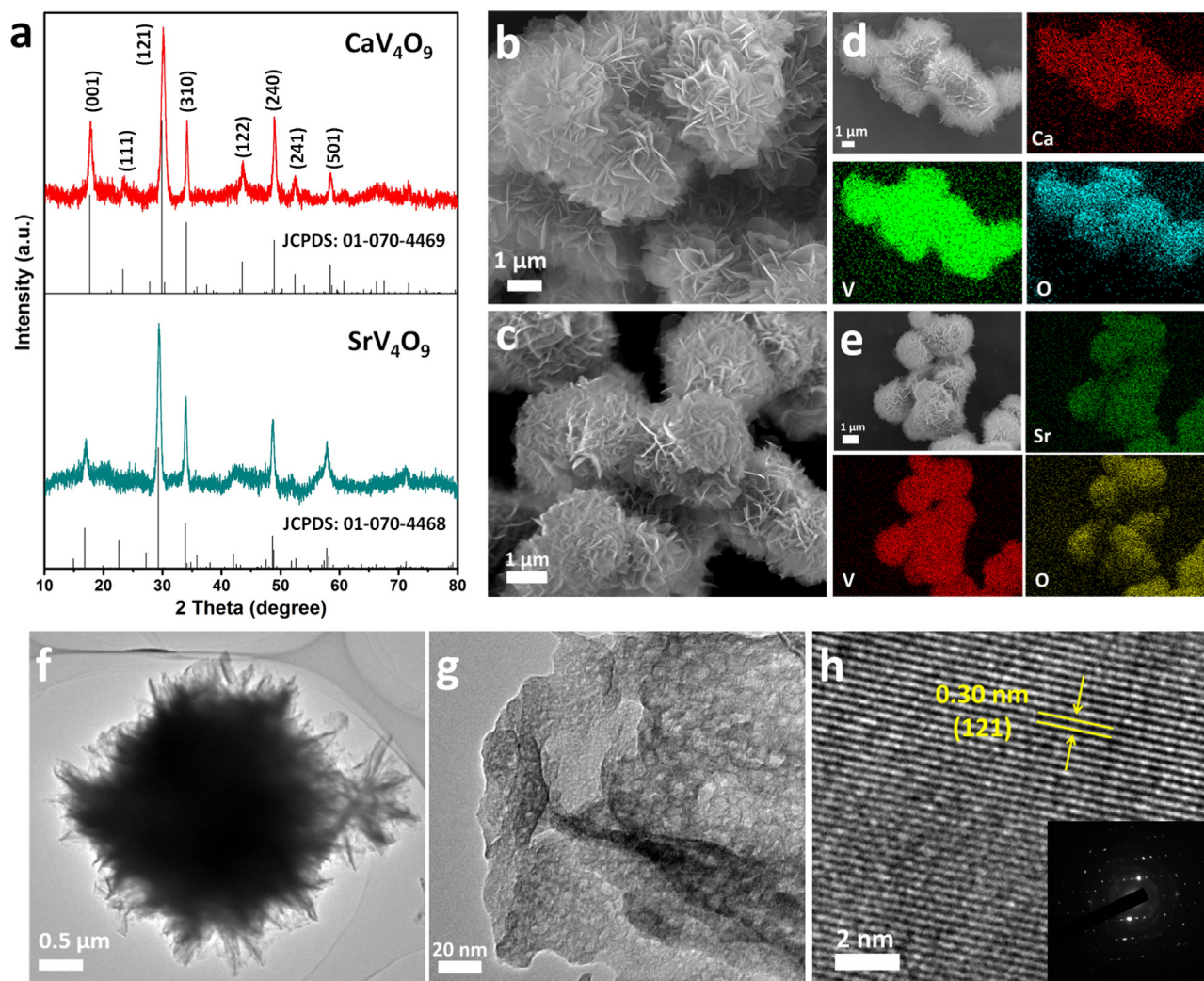


**Fig. 1.** Characterization of compact  $\text{CaV}_4\text{O}_9$  and  $\text{SrV}_4\text{O}_9$  microflowers. (a) XRD patterns of  $\text{CaV}_4\text{O}_9$  and  $\text{SrV}_4\text{O}_9$  microflowers. (b, c) SEM image of  $\text{CaV}_4\text{O}_9$  (b) and  $\text{SrV}_4\text{O}_9$  (c) microflowers. (d, e) EDS mappings of  $\text{CaV}_4\text{O}_9$  (d) and  $\text{SrV}_4\text{O}_9$  (e) microflowers. (f-h) TEM and HRTEM images of  $\text{CaV}_4\text{O}_9$  microflower; the inset of (h) is the SAED pattern.

observed in the nanosheets. The HRTEM image shows a distinct interplanar spacing of 0.30 nm (Fig. 1h), corresponding to the (121) lattice plane of  $\text{CaV}_4\text{O}_9$ . The selected area electron diffraction (SAED) pattern indicates the single crystalline nature of the nanosheets. The TEM and HRTEM images of  $\text{SrV}_4\text{O}_9$  microflower are displayed in Fig. S5, which exhibits the similar features to  $\text{CaV}_4\text{O}_9$ . The nitrogen adsorption-desorption measurement (Fig. S6) shows that BET surface areas for  $\text{CaV}_4\text{O}_9$  and  $\text{SrV}_4\text{O}_9$  microflowers are  $32.3 \text{ m}^2 \text{ g}^{-1}$  and  $31.6 \text{ m}^2 \text{ g}^{-1}$ , with an average pore diameter of 11.5 nm and 10.0 nm, respectively. We speculated that the formation of mesopores was caused by the decomposition of the glycerol or its derivative during the sintering process (as shown in Fig. S1). To confirm this, TGA and TEM were performed on the unsintered hydrothermal product of  $\text{CaV}_4\text{O}_9$ . TG curve shows a weight loss of 8.4% from 100° to 500°C under Ar atmosphere (Fig. S7). TEM images show that there are no distinct mesopores in the  $\text{CaV}_4\text{O}_9$  nanosheets before calcination (Fig. S8). Both of the results proved our speculation.

To understand the formation mechanism of the compact  $\text{CaV}_4\text{O}_9$  microflowers, time dependent experiments were carried out. SEM images of the samples obtained with different hydrothermal times were displayed in Fig. 2a–e and Fig. S9. It was found that microspheres with smooth surface were firstly generated at 1.0 h (Fig. 2a). When the time increased to 1.5 h, a large number of small nanoflakes were covered on the surface. Meanwhile, a spot of large nanosheets grown on the surface

were also observed (Fig. 2b). As the hydrothermal time increased to 2.0 h, the number of large nanosheets increased substantially (Fig. 2c). For the samples obtained at 3.0 h (Fig. 2d) and 6.0 h (Fig. S9), only large nanosheets can be observed to cover the surface, resulting in the formation of microflower-like structure. Such a morphology evolution from small nanoflakes to large nanosheets can be explained by the Ostwald Ripening mechanism. When the hydrothermal reaction further proceeded to 48 h, much denser microflowers were obtained (Fig. 2e). The detailed formation process was illustrated in Fig. 2f. ICP results show that the Ca/V ratio of the samples obtained at 1.5 h, 3.0 h and 48 h are 0.57/4, 0.92/4 and 1.07/4, respectively. The XRD patterns of the samples at different hydrothermal time were also collected (Fig. 2g). It was found that the sample obtained at 1.5 h only shows two weak peaks at about 26.1° and 50.3°. As the reaction proceeded to 3.0 h, another two peaks at about 30.1°, 34.2° appeared, and the peak at 50.3° shifted to 48.9°. Note that the three peaks at 30.1°, 34.2° and 48.9° are consistent with the diffraction peaks of (121), (310) and (240) planes of  $\text{CaV}_4\text{O}_9$ , respectively. However, the (001) reflection at about 17.6°, which is the characteristic of the layered structure, was not observed at this stage. These results suggest V-O chains were firstly formed at 1.5 h, and then converted to V-O layers with Ca ions adsorbed on the surface when the hydrothermal time increased to 3.0 h (Fig. 2h). This process can also be supported by the morphology transformation from small-sized nanoflakes at 1.5 h (Fig. 2b) to large-sized nanosheets at 3.0 h

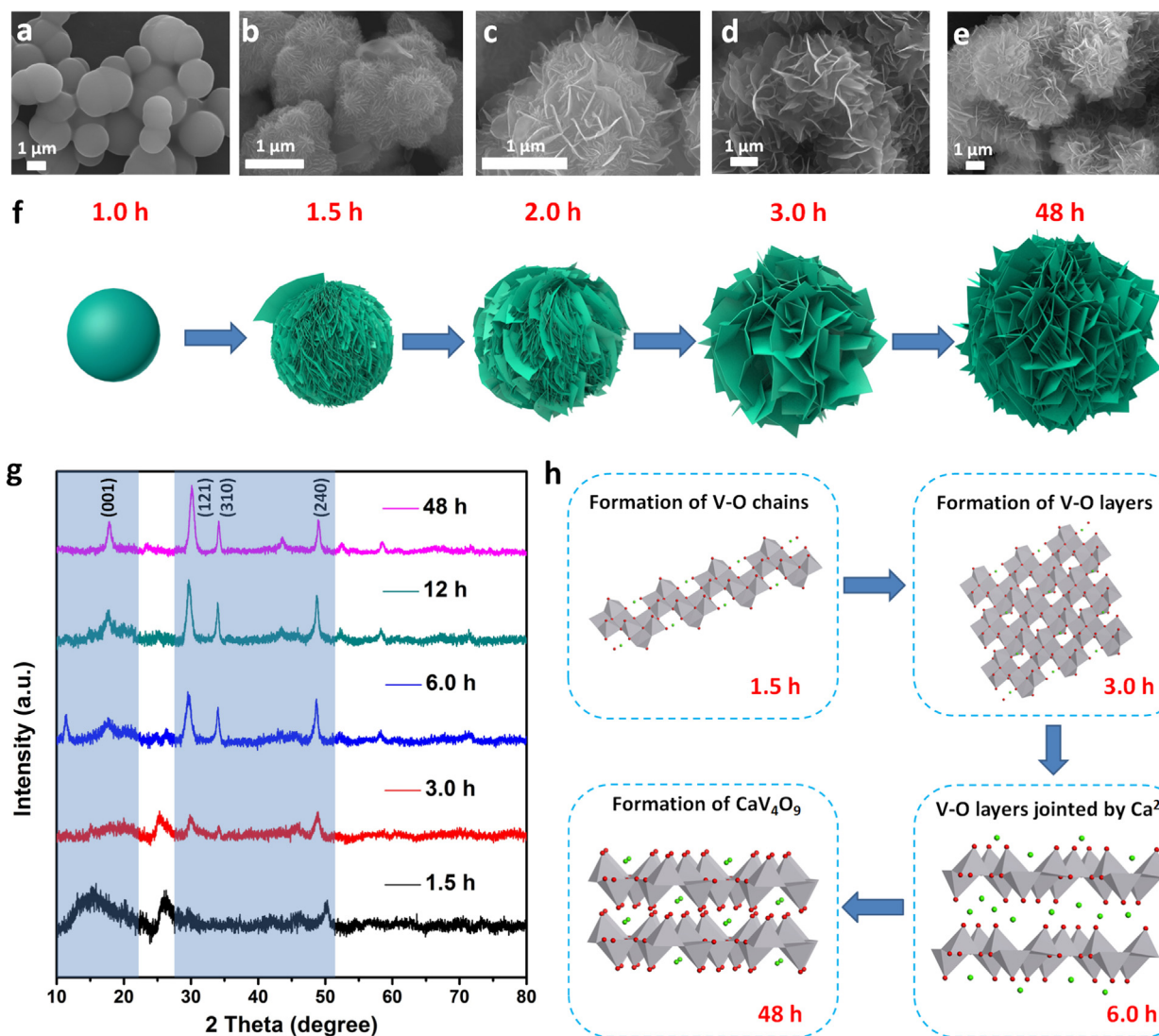


Fig. 2. (a–e) SEM images of the Ca-V-O samples obtained at different hydrothermal time. (f) Illustration of the formation process of compact CaV<sub>4</sub>O<sub>9</sub> microflower. (g) XRD patterns of the Ca-V-O samples obtained at different hydrothermal time. (h) Formation mechanism of the layered CaV<sub>4</sub>O<sub>9</sub> phase.

(Fig. 2d). When the time increased to 6.0 h, a new peak at the low angle of 11.6° was observed, suggesting that the V-O layers began to be joined by Ca<sup>2+</sup> and form a metastable layered structure with a large layer spacing (Fig. 2h). As time increased to 12 h and further to 48 h, the peak at 11.6° disappeared while the (001) peak at 17.6° appeared and became stronger (Fig. 2g), indicating the formation of the stable phase of CaV<sub>4</sub>O<sub>9</sub>.

To evaluate the Li storage properties of the compact CaV<sub>4</sub>O<sub>9</sub> microflowers, rate capability was firstly measured at different current density from 0.1 A g<sup>-1</sup> to 5.0 A g<sup>-1</sup> at the voltage range of 0.01–3.0 V vs. Li<sup>+</sup>/Li (Fig. 3a and b). It should be noted that the Li storage properties of CaV<sub>4</sub>O<sub>9</sub> has never been investigated previously. A high reversible capacity of ~700 mAh g<sup>-1</sup> was achieved with an initial Coulombic efficiency of 73.5% at the current density of 0.1 A g<sup>-1</sup>. When the current density increased to 5.0 A g<sup>-1</sup>, an average capacity of ~330 mAh g<sup>-1</sup> was maintained. A good recovery was observed at the second circulation from 0.1 A g<sup>-1</sup> to 5.0 A g<sup>-1</sup> and finally to 1.0 A g<sup>-1</sup>, with no distinct capacity decay after 300 cycles (Fig. 3b). These results indicate the excellent rate capability and cycling stability of the compact CaV<sub>4</sub>O<sub>9</sub> microflowers as LIB anode.

A high mass loading is necessary for the electrodes to get high areal capacity in practical applications [1,26]. Therefore, the electrochemical performance of an electrode material at high mass loadings is very

important and instructive for its commercialization potential. The long-term cycling performance of CaV<sub>4</sub>O<sub>9</sub> microflowers at a relatively high mass loading of 2.15 mg cm<sup>-2</sup> at a high current density of 1.0 A g<sup>-1</sup> is shown in Fig. S10. Stable cycling for 1000 cycles was achieved, further indicating the superior long-term cycling stability. Fig. 3c displays the achieved areal capacity of the compact CaV<sub>4</sub>O<sub>9</sub> microflowers at different mass loadings. A stable areal capacity of ~0.6 mAh cm<sup>-2</sup> and ~1.2 mAh cm<sup>-2</sup> were displayed at a mass loading of 0.76 mg cm<sup>-2</sup> and 1.74 mg cm<sup>-2</sup>, respectively. When the mass loading increased to 4.4 mg cm<sup>-2</sup>, a high reversible areal capacity of ~2.5 mAh cm<sup>-2</sup> at a current density of 0.02 A g<sup>-1</sup> (~0.1 mA cm<sup>-2</sup>) was achieved. Note that the achieved areal capacity can be comparable to or even higher than some reported areal capacities about Si anode [33–37], even though the gravimetric specific capacity of CaV<sub>4</sub>O<sub>9</sub> microflowers is lower than that of Si. Furthermore, as Fig. 3d shows, at a relatively high mass loading level of 3.42 mg cm<sup>-2</sup>, the stable cycling over 400 cycles at 0.5 A g<sup>-1</sup> (1.71 mA cm<sup>-2</sup>) was also demonstrated, with a stable areal capacity of ~1.56 mAh cm<sup>-2</sup>. As far as we know, the demonstrated stable cycling over 400 cycles with a high areal capacity has rarely been reported for high capacity LIB anodes (Table S2) [4,16,33–40]. These achievements, including high gravimetric capacity (~700 mAh g<sup>-1</sup>), high areal capacity (~2.5 mAh cm<sup>-2</sup>) and stable cycling performance (over 400 cycles) at high mass loadings (> 3.4 mg cm<sup>-2</sup>) of CaV<sub>4</sub>O<sub>9</sub> microflowers

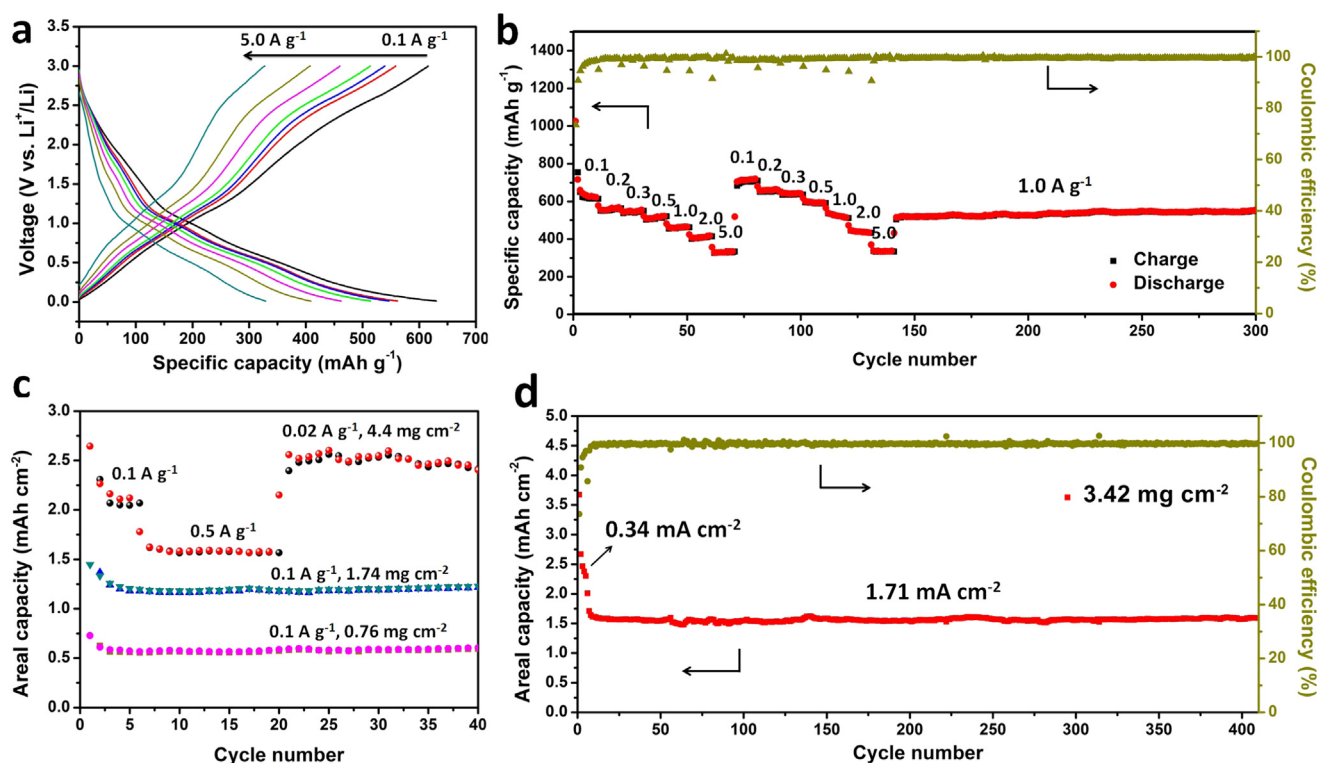


**Fig. 3.** Lithium storage performance of the compact  $\text{CaV}_4\text{O}_9$  microflowlers. (a) Charge/discharge profiles of  $\text{CaV}_4\text{O}_9$  microflowlers at different current densities. (b) Rate performance of  $\text{CaV}_4\text{O}_9$  microflowlers at a mass loading of  $0.98 \text{ mg cm}^{-2}$ . (c) Achieved areal capacity of  $\text{CaV}_4\text{O}_9$  microflowlers at different mass loadings. (d) Long-term cycling performance with areal capacity of  $\text{CaV}_4\text{O}_9$  microflowlers at a high mass loading of  $3.42 \text{ mg cm}^{-2}$ .

as LIB anode, are highly significant for the investigation and development of high-performance LIB anodes.

The sodium storage properties of the compact  $\text{CaV}_4\text{O}_9$  microflowlers were also investigated. Rate capability was firstly measured at different current densities from  $0.05 \text{ A g}^{-1}$  to  $5.0 \text{ A g}^{-1}$  at the voltage range of  $0.01\text{--}3.0 \text{ V vs. Na}^+/\text{Na}$ . The discharge/charge curves show sloping profiles without voltage plateau (Fig. 4a), which is consistent with our previous results [30]. Note that the discharge/charge profiles for Na storage are different from that for Li storage, which was also confirmed by the CV results (Fig. S11), suggesting the different reaction mechanism. A reversible capacity of  $\sim 320 \text{ mAh g}^{-1}$  with an initial Coulombic efficiency of 66.9% was achieved at a current density of  $0.05 \text{ A g}^{-1}$ , and  $\sim 143 \text{ mAh g}^{-1}$  was remained at the high current density of  $5.0 \text{ A g}^{-1}$  (Fig. 4b). Similar to the Li storage performance, a good recovery with no distinct capacity decay after 300 cycles was observed, indicating the excellent rate capability and cycling stability of compact  $\text{CaV}_4\text{O}_9$  microflowlers for Na storage.

To further investigate the cycling stability at a high current density in the case of different mass loadings, cycling performance was measured at a current density of  $1.0 \text{ A g}^{-1}$ . After 1000 cycles, high capacity retentions of 93.6% and 85.9% (relative to the 5th discharge capacity) were achieved at mass loadings of  $0.57 \text{ mg cm}^{-2}$  and  $1.44 \text{ mg cm}^{-2}$ , respectively (Fig. 4c), manifesting the superior long-term cycling stability of the prepared  $\text{CaV}_4\text{O}_9$  microflowlers. Fig. 4d shows the cycling stability with displayed areal capacity at different mass loadings. At the mass loadings of  $0.76$  and  $2.62 \text{ mg cm}^{-2}$ , stable areal capacity of  $0.25 \text{ mAh cm}^{-2}$  and  $0.64 \text{ mAh cm}^{-2}$  were achieved, respectively, without capacity fading after 100 cycles. When the mass loading increased to  $3.65 \text{ mg cm}^{-2}$ , the initial reversible areal capacity reached to  $\sim 1.0 \text{ mAh cm}^{-2}$ . After 100 cycles,  $0.82 \text{ mAh cm}^{-2}$  was remained, corresponding to a capacity retention of 82%. It should be pointed out that the current investigations about Na-ion batteries mainly focused on the electrochemical performance at low mass loading level with low areal capacity. Even though several works have reported high areal capacity

for SIB anodes, the results were achieved with special electrode modification, such as introducing considerable amounts of carbon nanotubes in the electrodes [41,42]. Here we just applied a typical coating method to prepare the electrode without any other special modification, which is more instructive to the scalable applications. In such cases, the achieved high areal capacity ( $\sim 1.0 \text{ mAh cm}^{-2}$ ) with the stable cycling has rarely been reported for Na-ion battery anodes (Table S3) [32,43–49].

The superior sodium storage performance of  $\text{CaV}_4\text{O}_9$  microflowlers in half cells inspired us to assemble sodium-ion full cells. We selected  $\text{Na}_3\text{V}_2(\text{PO}_4)_3$  (Fig. S12), a widely studied SIB cathode, to match with  $\text{CaV}_4\text{O}_9$  for full cell (Fig. S13a and S13b).  $\text{Na}_3\text{V}_2(\text{PO}_4)_3/\text{C}$  nanoparticles were prepared using our previously reported method [50]. Note that both cathode and anode are based on vanadium as the redox center (Fig. S13c), thus it can be called as all-vanadium sodium-ion full battery. The full cell was assembled using  $\text{CaV}_4\text{O}_9$  microflowlers as anode and excess  $\text{Na}_3\text{V}_2(\text{PO}_4)_3/\text{C}$  nanoparticles as cathode. The full cell displayed a sloping charge/discharge curves at a voltage range between  $0.5$  and  $3.2 \text{ V}$  with an average output voltage of  $\sim 1.7 \text{ V}$  (Fig. S13b). Good cycling stability of the full cell for 200 cycles was demonstrated at a high current density of  $1.0 \text{ A g}^{-1}$  (Fig. S13d).

To investigate and compare the Li storage and Na storage mechanism of  $\text{CaV}_4\text{O}_9$  microflowler, ex situ TEM analyses were carried out. At the sodiation state after 10 cycles (Fig. 5a–c), HRTEM image indicates the generation of small nanograins with a lattice fringe of  $0.21 \text{ nm}$  (Fig. 5b), which can be assigned to the (104) plane of  $\text{NaVO}_2$ . The SAED pattern displays two distinct diffraction rings with corresponding spacing of  $0.21 \text{ nm}$  and  $0.145 \text{ nm}$  (Fig. 5c), which correspond to (104) plane of  $\text{NaVO}_2$  and (311) plane of  $\text{CaO}$ , respectively. Therefore, the HRTEM image and SAED pattern manifest that  $\text{NaVO}_2$  and  $\text{CaO}$  nanograins with amorphous region were generated at the sodiation state, consistent with our previous demonstration and indicate the following Na storage mechanism [30]:

The initial sodiation process:

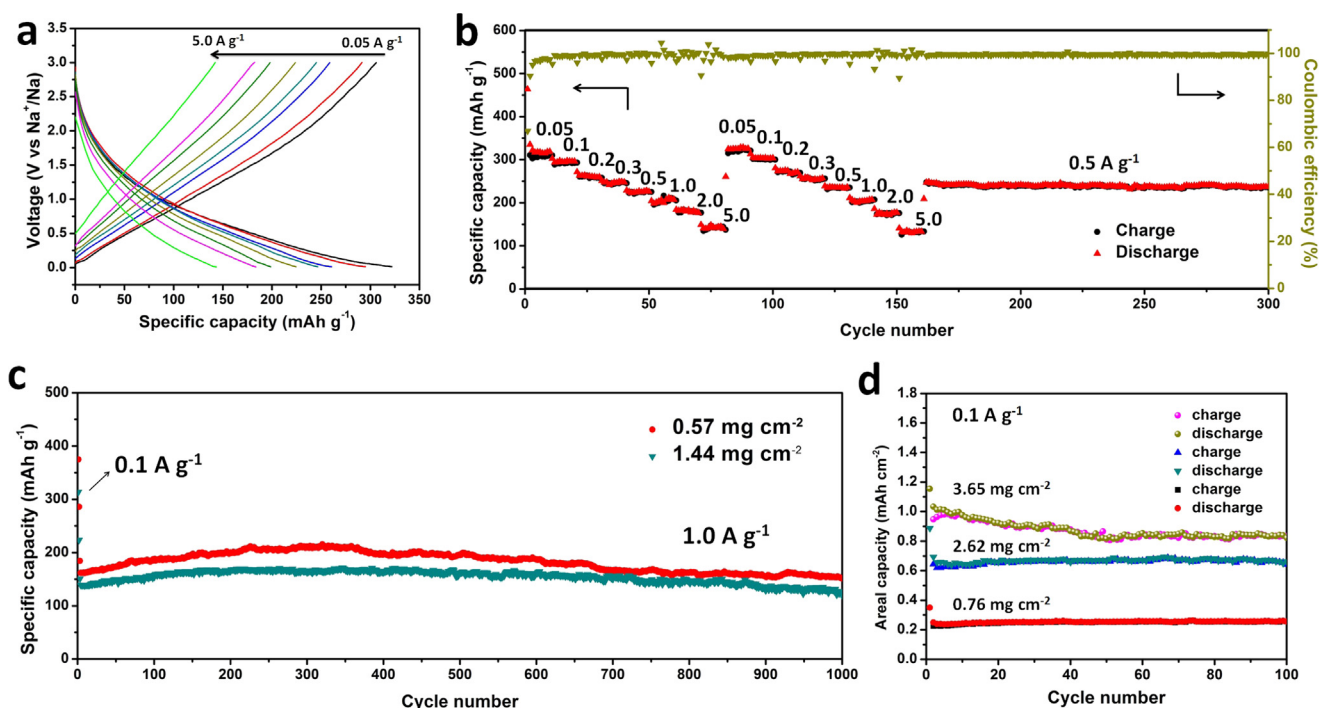
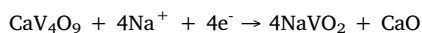
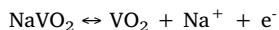


Fig. 4. Sodium storage performance of the compact  $\text{CaV}_4\text{O}_9$  microflowers. (a) Charge/discharge profiles of  $\text{CaV}_4\text{O}_9$  microflowers at different current densities. (b) Rate performance of  $\text{CaV}_4\text{O}_9$  microflowers at a mass loading of  $0.98 \text{ mg cm}^{-2}$ . (c) Long-term cycling performance of  $\text{CaV}_4\text{O}_9$  microflowers at  $1.0 \text{ A g}^{-1}$  with mass loadings of  $0.57 \text{ mg cm}^{-2}$  and  $1.44 \text{ mg cm}^{-2}$ , respectively. (d) Areal capacity and cycling performance of  $\text{CaV}_4\text{O}_9$  microflowers at different mass loadings.



The subsequent sodiation/desodiation cycles:



Our previous investigation has clearly demonstrated that the above reaction process was accompanied by only a tiny volume variation below 10%. Meanwhile, the in situ generated CaO nanograins provide a self-preserving effect to prevent the agglomeration of the active component,

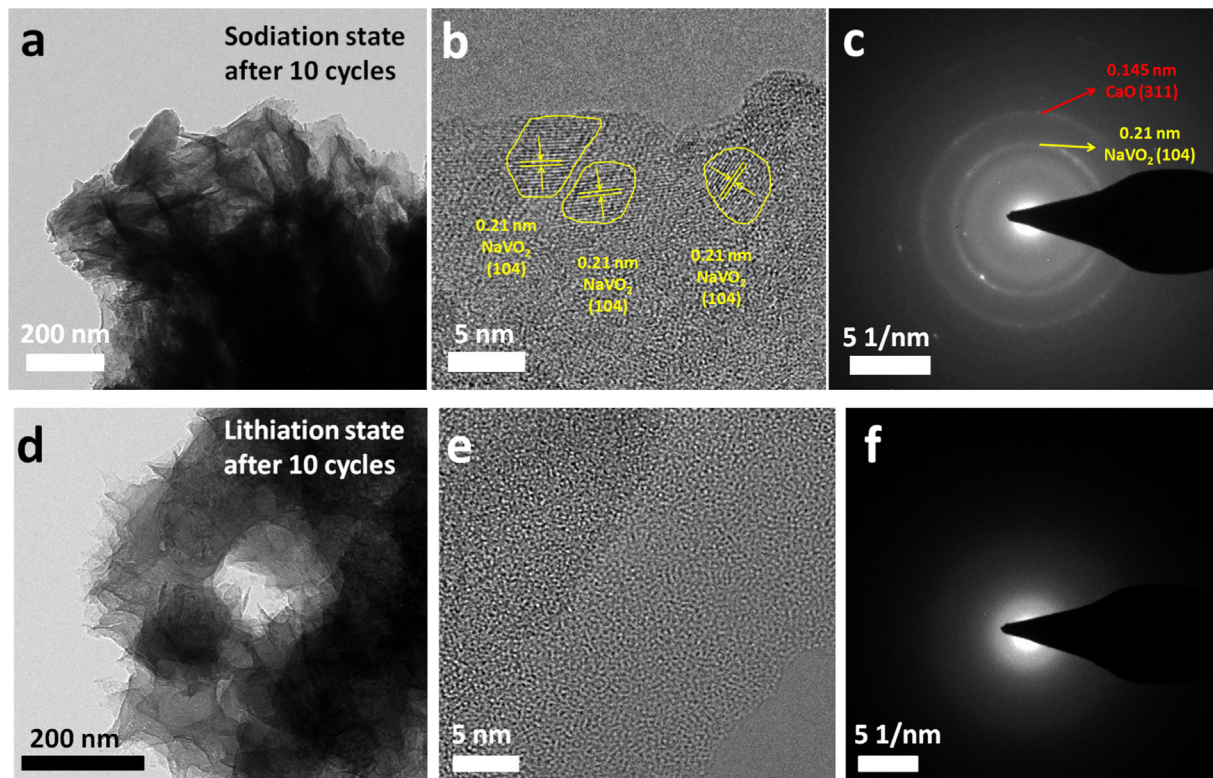


Fig. 5. Ex situ TEM measurements of  $\text{CaV}_4\text{O}_9$  microflower at the sodiation state and lithiation state after 10 cycles, respectively. (a-c) TEM image, HRTEM image and SAED pattern at the sodiation state. (d-f) TEM image, HRTEM image and SAED pattern at the lithiation state.

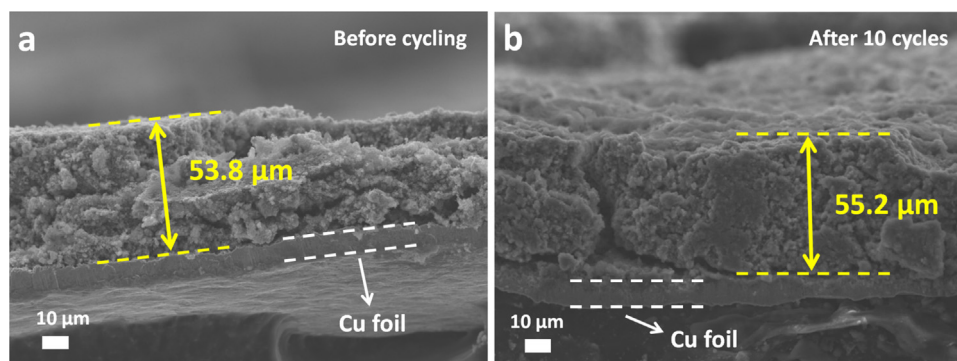


Fig. 6. Cross-sectional SEM images of  $\text{CaV}_4\text{O}_9$  microflower electrodes at high mass loading of  $3.83 \text{ mg cm}^{-2}$ . (a) Before cycling; (b) After 10 cycles for Li storage.

and thus keep the electrode with high reversibility. These superior properties together with the nanosheet-assembled microflower structure benefit to the charge transport property and electrode stability at high mass loadings.

Differently, for the lithiation state of  $\text{CaV}_4\text{O}_9$  microflowers after 10 cycles (Fig. 5d–f), the HRTEM image and SAED pattern indicate a totally amorphous form of the nanosheets (Fig. 5e and f), manifesting the different reaction mechanism for Li storage compared to Na storage. But it is noted that the nanosheets were well-maintained at the lithiation state, suggesting the small volume change properties of  $\text{CaV}_4\text{O}_9$  for Li storage as well. To confirm this point, ex situ SEM measurements were carried out. It was found that the microflower morphology was well preserved even after 500 cycles (Fig. S14), manifesting the structure stability of  $\text{CaV}_4\text{O}_9$  for Li storage. Moreover, the electrode stability was also investigated. Fig. 6 displays the cross-sectional SEM image of the electrode before and after 10 cycles. Notably, even though at a high mass loading level of  $3.83 \text{ mg cm}^{-2}$ , the thickness of the electrode only changed from  $\sim 53.8 \mu\text{m}$  before cycling to  $\sim 55.2 \mu\text{m}$  after cycles, further demonstrating the small volume change property of  $\text{CaV}_4\text{O}_9$  for Li storage and also, explaining the observed outstanding cycling stability of the compact  $\text{CaV}_4\text{O}_9$  microflower at high mass loadings. Even though the more detailed Li storage mechanism of  $\text{CaV}_4\text{O}_9$  may need to be further studied, the present results indicate that  $\text{CaV}_4\text{O}_9$  is a promising anode material for LIBs with both high capacity and small volume change.

Based on the above analyses, the achieved stable cycling performance with a high areal capacity of the nanosheet-assembled compact  $\text{CaV}_4\text{O}_9$  microflower for Li/Na storage can be ascribed to the following points: First, the intrinsic small volume change and the self-preserving effect from in situ generated CaO (in the case of Na storage) benefit to the structure stability and high reversibility of the electrodes during cycling; Second, the solid and compact microflower structure of  $\text{CaV}_4\text{O}_9$  exhibits an increased tap density ( $0.74 \text{ g cm}^{-3}$ ) compared to the nanowires or hollow nanostructures, which benefits to decrease the thickness of the electrodes and then reduce the charge transport pathway, especially at high mass loadings. Besides, the assembled nanosheets maintain the nano-effects including short ion diffusion distance, better strain release and good electrolyte infiltration. All these superior properties endow the as-prepared  $\text{CaV}_4\text{O}_9$  microflowers with a great potential for high performance LIB and SIB anodes.

#### 4. Conclusion

In summary, a facile method was firstly demonstrated to fabricate both solid  $\text{CaV}_4\text{O}_9$  and  $\text{SrV}_4\text{O}_9$  microflowers, and the detailed formation mechanism of the  $\text{CaV}_4\text{O}_9$  microflower was revealed. The prepared  $\text{CaV}_4\text{O}_9$  microflower was demonstrated to exhibit stable cycling performance with high areal capacity at high mass loadings, both for LIBs and SIBs. The superior electrochemical performance is attributed to: 1) The  $\text{CaV}_4\text{O}_9$  phase shows intrinsic small volume change during charge/

discharge; 2) the prepared compact microflower structure exhibits an increased tap density, benefiting to decrease the anode thickness; 3) the assembled nanosheets maintain the nano-effects for favorable electrochemical reaction. This work suggests  $\text{CaV}_4\text{O}_9$  or other alkaline earth metal vanadates are promising candidates for LIB and SIB anodes. Besides, the design of nanosheet-assembled compact microflowers provides an effective way to both increase the tap density of electrodes and maintain the nano-effects to assure the good electrochemical performance. More importantly, we believe the achievements about the stable cycling performance with high areal capacity will play positive impacts on the development of LIB/SIB anodes, and thus promote the innovation of battery technology.

#### Acknowledgements

This work was supported by the National Natural Science Fund for Distinguished Young Scholars (51425204), the National Natural Science Foundation of China (51521001), the National Key Research and Development Program of China (2016YFA0202603), the Programme of Introducing Talents of Discipline to Universities (B17034), the Yellow Crane Talent (Science & Technology) Program of Wuhan City and the Fundamental Research Funds for the Central Universities (WUT: 2016III001, 2017IVA100, 2017IVA096, 2017III009, 2017III040).

#### Appendix A. Supporting information

Supplementary data associated with this article can be found in the online version at <http://dx.doi.org/10.1016/j.nanoen.2018.06.012>.

#### References

- [1] H. Sun, L. Mei, J. Liang, Z. Zhao, C. Lee, H. Fei, M. Ding, J. Lau, M. Li, C. Wang, *Science* 356 (2017) 599–604.
- [2] R. Hu, Y. Ouyang, T. Liang, H. Wang, J. Liu, J. Chen, C. Yang, L. Yang, M. Zhu, *Adv. Mater.* 29 (2017) 1605006.
- [3] K. Zhao, M. Wen, Y. Dong, L. Zhang, M. Yan, W. Xu, C. Niu, L. Zhou, Q. Wei, W. Ren, *Adv. Energy Mater.* 7 (2017) 1601582.
- [4] R. Yi, J. Zai, F. Dai, M.L. Gordin, D. Wang, *Nano Energy* 6 (2014) 211–218.
- [5] Y. Sun, N. Liu, Y. Cui, *Nat. Energy* 1 (2016) 16071.
- [6] N. Yabuuchi, K. Kubota, M. Dahbi, S. Komaba, *Chem. Rev.* 114 (2014) 11636–11682.
- [7] X. Xu, M. Yan, X. Tian, C. Yang, M. Shi, Q. Wei, L. Xu, L. Mai, *Nano Lett.* 15 (2015) 3879–3884.
- [8] M. Gu, A. Kushima, Y. Shao, J.G. Zhang, J. Liu, N.D. Browning, J. Li, C. Wang, *Nano Lett.* 13 (2013) 5203–5211.
- [9] H. Wu, G. Chan, J.W. Choi, I. Ryu, Y. Yao, M.T. McDowell, S.W. Lee, A. Jackson, Y. Yang, L. Hu, *Nat. Nanotechnol.* 7 (2012) 310–315.
- [10] Y.X. Wang, J. Yang, S.L. Chou, H.K. Liu, W.X. Zhang, D. Zhao, S.X. Dou, *Nat. Commun.* 6 (2015) 8689.
- [11] L. Yu, H. Hu, H.B. Wu, X.W. Lou, *Adv. Mater.* 29 (2017) 1604563.
- [12] Q. Wei, F. Xiong, S. Tan, L. Huang, E.H. Lan, B. Dunn, L. Mai, *Adv. Mater.* 29 (2017) 1602300.
- [13] L. Zhou, Z. Zhuang, H. Zhao, M. Lin, D. Zhao, L. Mai, *Adv. Mater.* 29 (2017) 1602914.

- [14] J. Liang, X.Y. Yu, H. Zhou, H.B. Wu, S. Ding, X.W. Lou, *Angew. Chem.* 53 (2014) 12803–12807.
- [15] J. Liang, H. Hu, H. Park, C. Xiao, S. Ding, U. Paik, X.W. Lou, *Energy Environ. Sci.* 8 (2015) 1707–1711.
- [16] N. Liu, Z. Lu, J. Zhao, M.T. McDowell, H.W. Lee, W. Zhao, Y. Cui, *Nat. Nanotechnol.* 9 (2014) 187–192.
- [17] C. Kim, G. Hwang, J.W. Jung, S.H. Cho, J.Y. Cheong, S. Shin, S. Park, I.D. Kim, *Adv. Funct. Mater.* 27 (2017) 1605975.
- [18] Y. Jiang, Y. Li, P. Zhou, Z. Lan, Y. Lu, C. Wu, M. Yan, *Adv. Mater.* 29 (2017) 1606499.
- [19] K. Zhao, L. Zhang, R. Xia, Y. Dong, W. Xu, C. Niu, L. He, M. Yan, L. Qu, L. Mai, *Small* 12 (2016) 588–594.
- [20] J. Yang, S. Li, A. Kushima, X. Zheng, Y. Sun, X. Jin, S. Jie, W. Xue, G. Zhou, W. Jiang, *Energy Environ. Sci.* 10 (2017) 580–592.
- [21] Y. Liu, N. Zhang, L. Jiao, J. Chen, *Adv. Mater.* 27 (2015) 6702–6707.
- [22] N. Zhang, X. Han, Y. Liu, X. Hu, Q. Zhao, J. Chen, *Adv. Energy Mater.* 5 (2014) 1401123.
- [23] J. Sun, H.W. Lee, M. Pasta, H. Yuan, G. Zheng, Y. Sun, Y. Li, Y. Cui, *Nat. Nanotechnol.* 10 (2015) 980–985.
- [24] G. Zou, H. Hou, G. Zhao, P. Ge, D. Yin, X. Ji, J. Mater. Chem. A 6 (2018) 4839–4847.
- [25] Y. Dai, Q. Li, S. Tan, Q. Wei, Y. Pan, X. Tian, K. Zhao, X. Xu, Q. An, L. Mai, *Nano Energy* 40 (2017) 73–81.
- [26] K.G. Gallagher, S.E. Trask, C. Bauer, T. Woehle, S.F. Lux, M. Tschech, P. Lamp, B.J. Polzin, S. Ha, B. Long, *J. Electrochem. Soc.* 163 (2016) A138–A149.
- [27] M. Singh, J. Kaiser, H. Hahn, *J. Electrochem. Soc.* 162 (2015) A1196–A1201.
- [28] O.B. Chae, J. Kim, I. Park, H. Jeong, J.H. Ku, H.R. Ji, K. Kang, S.M. Oh, *Chem. Mater.* 26 (2014) 5874–5881.
- [29] J. Yao, Y. Lia, R.C. Massé, E. Uchaker, G. Cao, *Energy Storage Mater.* 11 (2018) 205–259.
- [30] X. Xu, C. Niu, M. Duan, X. Wang, L. Huang, J. Wang, L. Pu, W. Ren, C. Shi, J. Meng, *Nat. Commun.* 8 (2017) 460.
- [31] M. Yoshio, H. Wang, K. Fukuda, T. Umeno, T. Abe, Z. Ogumi, *J. Mater. Chem.* 14 (2004) 1754–1758.
- [32] Y. Wen, K. He, Y. Zhu, F. Han, Y. Xu, I. Matsuda, Y. Ishii, J. Cumings, C. Wang, *Nat. Commun.* 5 (2014) 4033.
- [33] X. Li, M. Gu, S. Hu, R. Kennard, P. Yan, X. Chen, C. Wang, M.J. Sailor, J.G. Zhang, J. Liu, *Nat. Commun.* 5 (2014) 4105.
- [34] Q. Xiao, Y. Fan, X. Wang, R.A. Susantyoko, Q. Zhang, *Energy Environ. Sci.* 7 (2014) 655–661.
- [35] W. Si, X. Sun, X. Liu, L. Xi, Y. Jia, C. Yan, O.G. Schmidt, *J. Power Sources* 267 (2014) 629–634.
- [36] Q. Zhang, H. Chen, L. Luo, B. Zhao, H. Luo, X. Han, J. Wang, C. Wang, Y. Yang, T. Zhu, *Energy Environ. Sci.* 11 (2018) 669–681.
- [37] D. Lin, Z. Lu, P.C. Hsu, H.R. Lee, N. Liu, J. Zhao, H. Wang, C. Liu, Y. Cui, *Energy Environ. Sci.* 8 (2015) 2371–2376.
- [38] W. Zeng, F. Zheng, R. Li, Y. Zhan, Y. Li, J. Liu, *Nanoscale* 4 (2012) 2760–2765.
- [39] X. Wang, Y. Fan, R.A. Susantyoko, Q. Xiao, L. Sun, D. He, Q. Zhang, *Nano Energy* 5 (2014) 91–96.
- [40] Y. Li, K. Yan, H.W. Lee, Z. Lu, N. Liu, Y. Cui, *Nat. Energy* 1 (2016) 15029.
- [41] Y. Liu, X. He, D. Hanlon, A. Harvey, J.N. Coleman, Y. Li, *ACS Nano* 10 (2016) 8821–8828.
- [42] H. Ye, L. Wang, S. Deng, X. Zeng, K. Nie, P.N. Duchesne, B. Wang, S. Liu, J. Zhou, F. Zhao, *Adv. Energy Mater.* 7 (2016) 1601602.
- [43] P. Liu, Y. Li, Y.S. Hu, H. Li, L. Chen, X. Huang, *J. Mater. Chem. A* 4 (2016) 13046–13052.
- [44] Y. Zhang, C.W. Foster, C.E. Banks, L. Shao, H. Hou, G. Zou, J. Chen, Z. Huang, X. Ji, *Adv. Mater.* 28 (2016) 9391–9399.
- [45] F. Xie, L. Zhang, D. Su, M. Jaroniec, S.Z. Qiao, *Adv. Mater.* 29 (2017) 1700989.
- [46] Y. Chen, X. Hu, B. Evanko, X. Sun, X. Li, T. Hou, S. Cai, C. Zheng, W. Hu, G.D. Stucky, *Nano Energy* 46 (2018) 117–127.
- [47] H. He, Q. Gan, H. Wang, G.-L. Xu, X. Zhang, D. Huang, F. Fu, Y. Tang, K. Amine, M. Shao, *Nano Energy* 44 (2018) 217–227.
- [48] G. Wang, J. Zhang, S. Yang, F. Wang, X. Zhuang, K. Müllen, X. Feng, *Adv. Energy Mater.* (2017) 1702254.
- [49] X. Yang, R.Y. Zhang, J. Zhao, Z.X. Wei, D.X. Wang, X.F. Bie, Y. Gao, J. Wang, F. Du, G. Chen, *Adv. Energy Mater.* (2017) 1701827.
- [50] W. Ren, X. Yao, C. Niu, Z. Zheng, K. Zhao, Q. An, Q. Wei, M. Yan, L. Zhang, L. Mai, *Nano Energy* 28 (2016) 216–223.



**Peijie Wu** received his B.S. degree in International School of Materials Science and Engineering from Wuhan University of Technology (WUT) in 2017. He is currently working toward the M.S. degree and his current research focuses on energy storage materials and devices.



**Qi Li** is an Associate Professor of Materials Science and Engineering at Wuhan University of Technology (WUT). She received her Ph.D. degree from the University of Melbourne in 2007. Currently, her research interests focused on electrochemical energy storage and conversion.



**Wei Yang** received his M.S. degree in Materials Engineering from Wuhan University of Technology in 2017. He is currently a research assistant at Wuhan University of Technology. His research interests focus on developing functional materials for micro energy storage devices.



**Xiao Zhang** received his B.S. degree in School of Materials Science and Engineering from Liaocheng University. He is currently working toward the M.S. degree in Wuhan University of Technology. His current research focuses on energy storage materials and devices.



**Xuanpeng Wang** received his M.S. degree from Wuhan University of Technology in 2016. He is currently working toward the Ph.D. degree in Wuhan University of Technology and his current research focuses on the energy storage materials and devices.



**Xiaoming Xu** received his B.S. degree in Material Science and Engineering from Wuhan University of Technology (WUT) in 2014. He is currently working toward the Ph.D. degree and his current research focuses on vanadium-based nanomaterials for emerging energy storage.



**Jiashen Meng** received his B.S. degree from Wuhan University of Technology in 2015. He is currently working toward the Ph.D degree in Wuhan University of Technology and his current research focuses on the energy conversion and storage materials.



**Liqiang Mai** is Chair Professor of Materials Science and Engineering at Wuhan University of Technology (WUT). He is Changjiang Scholar Professor, Distinguished Young Scholar of the National Science Fund of China. He received his Ph.D. from WUT in 2004 and carried out his post-doctoral research in the laboratory of Prof. Zhonglin Wang at Georgia Institute of Technology in 2006–2007. He worked as advanced research scholar in the laboratory of Prof. Charles M. Lieber at Harvard University in 2008–2011 and Prof. Peidong Yang's group at University of California, Berkeley in 2017. His current research interests focus on nanomaterials and devices for energy storage.



**Chaojiang Niu** received his Ph.D. degree from Wuhan University of Technology (WUT) in 2016. He is now carrying out his postdoctoral research in the laboratory of Prof. Jun Liu at the Pacific Northwest National Laboratory (PNNL). His current research focuses on nano energy materials and devices, including rational material synthesis, control performance, device design, in-situ characterization for electrochemical energy storage.